

## FAR FIELD IMAGING RESEARCH BASED ON MULTILAYER POSITIVE- AND NEGATIVE-REFRACTIVE-INDEX MEDIA UNDER OFF-AXIS ILLUMINATION

P. F. Cao, X. P. Zhang, L. Cheng, and Q. Q. Meng

School of Information Science and Engineering  
Lanzhou University  
Lanzhou 730000, China

**Abstract**—In this work, a far field imaging model based on the array structure of positive- and negative-refractive-index media and modulation subwavelength-gratings is firstly presented and is named as the multilayer far field superlens (MLFSL). This new lens is capable of producing optical images by enhancing evanescent waves to the far field. The principle of MLFSL is discussed in detail, and the necessary and sufficient condition for designing MLFSL is obtained. Simultaneously, off-axis illumination technology is introduced to MLFSL system to further improve super-resolution, and the transfer matrix which contains the incident angle is obtained. The results demonstrate that, compared with other far field superlens, the subwavelength resolution of MLFSL has been enhanced. Such remarkable imaging capability of MLFSL promises new potential for nanoscale imaging and lithography.

### 1. INTRODUCTION

In 1967, Veselago [1] predicted that a planar slab of Left-Hand Materials (LHM), which possessed both negative permittivity and permeability, could refocus the electromagnetic waves from a point source. In 2000, Pendry [2] extended Veselago's analysis and further predicted that evanescent waves, which carry subwavelength structural information of the object, could be amplified inside the LHM slab and reconstructed in the image plane without loss in amplitude. Therefore the LHM slab can be used as a "superlens" to achieve super-resolution, which overcomes the diffraction limit of conventional imaging systems.

---

Corresponding author: X. Zhang (zxp@lzu.edu.cn).

So far, many approaches of imaging beyond the diffraction limit with superlens have been reported [3–14]. However, due to the intrinsic losses, the superlenses are only capable of projecting an image in the near field. In 2007, the far-field optical superlens (FSL) was presented by Liu et al. and Lee et al. [15,16], which can image in the far field. Refs. [15] and [16] show that the FSL consists of a grating structure and a flat silver slab. This is especially true that the high-frequency Fourier components can give the highest resolution to the far field image. Unfortunately, unless the lens is very close to the ideal lossless structure, these large fields will result in dissipation, caused by the intrinsic absorption of the LHM, which will stop the amplifying effect. Ramakrishna and Pendry [17] presented multilayer thin negative-material slabs to improve image resolution under surface plasmon resonances effect in the near field to overcome the intrinsic absorption. However, the intrinsic absorption effect of FSL in the far field is not resolved.

In this paper, a far field imaging model based on the array structure of positive- and negative-refractive-index media and modulation subwavelength-gratings is firstly presented to ameliorate the surface plasmon resonances effects and is termed as the MultiLayer Far Field SuperLens (MLFSL). MLFSL is composed of two arrays of multilayer thin silver slabs and periodic corrugations. The Off-Axis Illumination (OAI) technology [18, 19], which is introduced firstly into our MLFSL imaging system, is utilized to achieve better super-resolution in the far field. Thus, the transfer matrix is obtained, and it contains the incident angle of OAI. By analyzing and discussing the MLFSL imaging system, we acquire the necessary and sufficient condition for designing MLFSL. Simultaneously, the Optical Transfer Function (OTF) and light intensity distributions of MLFSL are compared with FSL [15,16]. These research results indicate that the super-resolution can be remarkably improved.

## 2. MULTILAYER FAR FIELD SUPERLENS

The proposed MLFSL is made of the stack of extremely thin superlens and periodic corrugations. Positioning of MLFSL in the vicinity of an object can significantly enhance the evanescent waves scattered by the object. Figure 1 shows the configuration of our MLFSL sample. The sample is comprised of two main parts: an object and a MLFSL. The MLFSL consists of two arrays of multilayer thin silver slabs and a modulated grating structure.

The principle of the MLFSL is: (i) The evanescent components are enhanced in near-field; (ii) these components are shifted into

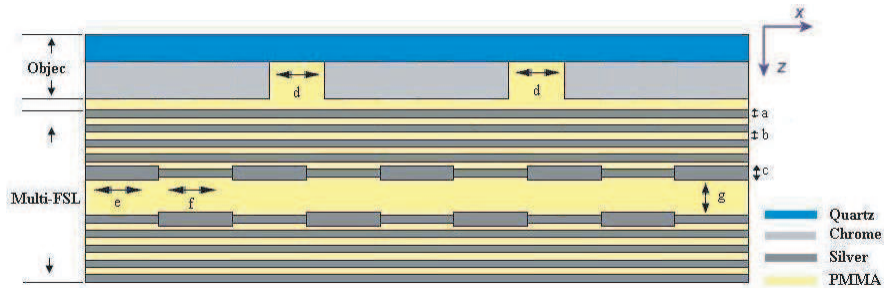


**Figure 1.** MLFSL sample structure.

the propagating bands by using periodic corrugations, and then the evanescent components can be propagated to far-field; (iii) evanescent bands are shifted back into their original locations in the far-field; (iv) the evanescent components are enhanced again. Finally, the evanescent bands are combined with the propagating band from an additional measurement for image reconstruction.

Both (i) and (iv) are progresses of enhancing evanescent waves; (ii) is progress of modulating evanescent waves into the propagating bands; (iii) is the inverse of (ii). We can analyze the performance of MLFSL by discussing (i) and (ii).

We use the array structure, which consists of the stack of alternating extremely thin layers of negative- and positive-refractive index media, to ameliorate the effects of dissipation. Subwavelength gratings can be used to convert evanescent waves into propagating waves by shifting their incident field wavevectors,  $k_{in}$ , into the various diffraction orders, i.e.,  $k = k_{in} + mk_{\Lambda}$ ;  $m$  is the diffraction order through the grating;  $\Lambda$  is the grating period [15]. The far-field signal at a given  $k$  is therefore a superposition of the various diffraction orders of waves. For example, incident waves with wavevectors  $k_1$ ,  $k$ , and  $k_2$  can be simultaneously mapped into a single propagating wave through the  $-1$ ,  $0$ , and  $+1$  diffraction orders, respectively. So the MLFSL can convert evanescent waves into propagating waves by shifting their incident field wavevectors into the various diffraction orders to achieve the super-resolution imaging in the far field.

Because it has been proved that the OAI can heighten  $\pm 1$  order diffraction waves [19], the transfer matrix method containing the incident angle is used to compute electromagnetic field distribution in each layer under oblique illumination. Let us assume that  $\vec{K}$  is the wave vector of the light source;  $\vec{k}$  is the diffraction wave vector,

$k_{xj} = K_x + \frac{2\pi}{\Lambda_{obj}}j$ ,  $K_x = \frac{2\pi}{\lambda} \sin \theta$ ;  $k_{zj}$  are the components of wave vector along the  $X$ -axis and  $Z$ -axis, respectively;  $j$  is an integer referring to a diffraction order;  $\Lambda_{obj}$  is the period of the object;  $\theta$  is the incident angle which is the intersection angle between the incident wave vector and  $Z$ -axis. Provided  $k_{xj}$  is given,  $k_{zj}$  is obtained by dispersion relation  $k_{xj}^2 + k_{zj}^2 = \varepsilon\mu\omega^2$ .

In order to increase the speed of calculation, the incident electromagnetic wave is divided into TE and TM polarizations to get their respective results, and the combination of them is the total outcome in truth. We first calculate the field components in TM polarization. Inside a stratified layer  $i$ , the magnetic fields are expressed by

$$\vec{H}_{j,i} = \left( H_{j,i}^+ + H_{j,i}^- \right) \vec{y} \quad (1)$$

where, for evanescent waves,  $H_{ji}^+$  and  $H_{ji}^-$  are the magnetic components of growth and attenuation in the negative- and positive-refractive-index media, respectively; while for propagation waves, they are the magnetic components in opposite propagation directions in the positive- and negative-refractive-index media, respectively.

When (1) is substituted back in Maxwell's equations, the electric fields in  $i$ -layer can be obtained

$$\vec{E}_{j,i} = \frac{k_{zj,i}}{\omega\varepsilon_i} \left( H_{j,i}^+ - H_{j,i}^- \right) \vec{x} - \frac{k_{xj}}{\omega\varepsilon_i} \left( H_{j,i}^+ + H_{j,i}^- \right) \vec{z} \quad (2)$$

By matching the boundary conditions, the tangential components of the electric and magnetic fields must be continuous at  $z = i$ . We obtain

$$\begin{bmatrix} H_{iy} \\ E_{ix} \end{bmatrix} = \begin{bmatrix} 1 & 1 \\ \frac{k_{zj,i}}{\omega\varepsilon_i} & -\frac{k_{zj,i}}{\omega\varepsilon_i} \end{bmatrix} \begin{bmatrix} H_{j,i}^+ \\ H_{j,i}^- \end{bmatrix} = D_i \begin{bmatrix} H_{j,i}^+ \\ H_{j,i}^- \end{bmatrix} \quad (3)$$

where  $D_i$  is defined as the transformation matrix, which contains the incident angle of OAI.

By matching the boundary conditions between  $i$ - and  $(i+1)$ -layers, the expression must be written as

$$\begin{bmatrix} H_{j,i}^+ \\ H_{j,i}^- \end{bmatrix} = D_i^{-1} D_{i+1} \begin{bmatrix} H_{j,(i+1)}^+ \\ H_{j,(i+1)}^- \end{bmatrix} \quad (4)$$

In the same layer, the magnetic components at the boundary of downgoing (+) and upgoing (-) can be expressed as

$$\begin{bmatrix} H_{j,i}^+ \\ H_{j,i}^- \end{bmatrix}_+ = \begin{bmatrix} e^{-jk_{zj,i}d_i} & 0 \\ 0 & e^{jk_{zj,i}d_i} \end{bmatrix} \begin{bmatrix} H_{j,i}^+ \\ H_{j,i}^- \end{bmatrix}_- = P_i \begin{bmatrix} H_{j,i}^+ \\ H_{j,i}^- \end{bmatrix}_- \quad (5)$$

where  $P_i$  is propagation matrix, and  $d_i$  is the thickness of  $i$ -layer.

Then the magnetic components at the  $i$ -layer of downgoing (+) can be rewritten

$$\begin{bmatrix} H_{j,i}^+ \\ H_{j,i}^- \end{bmatrix}_+ = P_i D_i^{-1} D_i \begin{bmatrix} H_{j,(i+1)}^+ \\ H_{j,(i+1)}^- \end{bmatrix}_- \quad (6)$$

Similarly, we can obtain

$$\begin{aligned} \begin{bmatrix} H_{j,1}^+ \\ H_{j,1}^- \end{bmatrix}_+ &= D_1^{-1} D_2 P_2 D_2^{-1} \dots D_{n-1}^{-1} P_{n-1} D_{n-1}^{-1} D_n \begin{bmatrix} H_{j,n}^+ \\ H_{j,n}^- \end{bmatrix}_- \\ &= M \begin{bmatrix} H_{j,n}^+ \\ H_{j,n}^- \end{bmatrix}_- \end{aligned} \quad (7)$$

where  $M$  is called as transfer matrix, and it is defined by the layer thickness and propagation constant. Since  $M$  contains the incident angle of OAI, the effect of the projection system parameters are introduced into the imaging process, which can improve super-resolution [19].

The electric components can be obtained by using electromagnetic field dual relations.

Next, we compute the period of subwavelength gratings, which can be used to convert evanescent waves into propagating waves by shifting their incident field wavevectors into the various diffraction orders. We only compute 0 and  $\pm 1$  diffraction orders in this paper. Now the corrugations field is assumed to be:

$$c(x) = 1 + \cos(2\pi k_\Lambda x + \phi_0) \quad (8)$$

where  $k_\Lambda$  is the spatial frequency of subwavelength gratings;  $\phi_0$  is the initial phase.

The evanescent waves distribution function is  $s(x)$ , then the distribution function after modulating is

$$r(x) = s(x) c(x) = s(x) [1 + \cos(2\pi k_\Lambda x + \phi_0)] \quad (9)$$

It is written as the spectrum function by Fourier Transform:

$$\begin{aligned} R(k_{xj}) &= S(k_{xj}) + \frac{1}{2} S(k_{xj} - k_\Lambda) e^{j\phi_0} + \frac{1}{2} S(k_{xj} + k_\Lambda) e^{-j\phi_0} \\ &= S(k_{xj}') + \frac{1}{2} S(k_{xj}') e^{j\phi_0} + \frac{1}{2} S(k_{xj}') e^{-j\phi_0} \end{aligned} \quad (10)$$

where  $k_{xj}' = k_{xj} + mk_\Lambda$  and  $m$  ( $m = 0, -1, 1$ ) is diffraction order through the grating. Evanescent waves are characterized by  $|k_{xj}| > k_c$ , and  $k_c$  is the upper limit of propagating band. So incident evanescent waves can be simultaneously mapped into a single propagating wave

through the 0,  $-1$ , and  $+1$  diffraction orders by using subwavelength gratings. Consequently, only transmitted waves with  $|k_{xj} \pm k_\Lambda| < k_c$  should be considered, and  $k_\Lambda \geq 2k_c$  is the necessary and sufficient condition for our MLFSL system.

Similarly, the evanescent waves in the far-field are obtained by inverse transforming of (10). When these evanescent and propagating waves are substituted back in (7), we can obtain the magnetic components at the image plane:

$$\begin{bmatrix} H_{img,1}^+ \\ H_{img,1}^- \end{bmatrix}_+ = M \begin{bmatrix} H_{img,n}^+ \\ H_{img,n}^- \end{bmatrix}_- \quad (11)$$

where  $M$  is the same as in Eq. (7).

Following the same method, the field components under TE polarization have similar expressions.

And the final intensity can be obtained by applying the definition of intensity [20]:

$$I = |\langle S \rangle| = \left| \frac{c}{16\pi} \left( \vec{E} \times \vec{H}^* + \vec{E}^* \times \vec{H} \right) \right| \quad (12)$$

Then, the transmittance is calculated by following expression:

$$T = \frac{\tilde{I}}{\tilde{I}_0} \quad (13)$$

where  $\tilde{I}$  is the normalization intensity, and  $\tilde{I}_0$  is the source intensity.

### 3. NUMERICAL SIMULATIONS

The softwares COMSOL Multiphysics and Matlab are used for simulation. In following figures, the units of  $x$  and  $z$  are meter. The object and MLFSL are shown in Figure 1, and the FSL is shown in [15]. Firstly, the negative-refractive material and range of wavelengths are discussed. In the visible wavelengths region, the permittivity of Ag can be approximated by the Drude model as follows

$$\varepsilon = \varepsilon' + i \cdot \varepsilon'' = \varepsilon_\infty - \frac{\omega_p^2}{\omega(\omega + i \cdot \Gamma)} \quad (14)$$

where  $\omega_p$  is the plasma frequency (9.01 eV for Ag) [21], the contribution of bounded electrons  $\varepsilon_\infty$ , relaxation constant  $\Gamma$ , and angular frequency  $\omega$  of the source. And magnetic permeability is characterized by [22]. In visible range, the permittivity and magnetic permeability of Ag are negative, and it is called left-handed material (LHM) because when an electromagnetic (EM) plane wave propagates in it, the direction of

Poynting vector will be opposite to that of wave-vector ( $k$ ) so that  $k$ ,  $E$ ,  $H$  form a left-handed set of vectors [1]. It is well known that the refractive index is responsible to the phase velocity of EM wave, and the refraction is related to the group velocity. So a clear awareness should be hold that the concept of negative refraction is not equal to that of negative refractive index. There is a negative refractive index  $n = k_{LHM}/k_0$  [23], where the direction of  $k_{LHM}$  is opposite to that of  $k_0$ . So refractive index in the LHM's is often defined as negative [2, 23, 24].

The image quality and focal position of superlens are strongly dependent on the absorption loss in materials, which is characterized by parameter  $\varepsilon'' (> 0)$  [21]. From Eq. (14), there are positive  $\varepsilon''$  and negative  $\varepsilon'$  in the visible frequency range, so we need to select optimized wavelength to compensate for the blurring due to intrinsic absorption loss. The integrated mean intensity of the multilayer Ag slabs superlens versus the propagation distance along  $z$  direction is also shown in Figure 2.  $\varepsilon'$  can be changed by tuning the wavelength of the incident light for imaging as shown in Table 1. From Figure 2 and Table 1, at 335 nm wavelength, the intensity attenuates most slowly, and the focal spot size is the biggest. So 335 nm wavelength is selected as incident wavelength.

**Table 1.** The wavelength, focal spot sizes, versus various  $\varepsilon'$  of Ag.

wavelengths (nm)	331	332	335	341
$\varepsilon'$	-0.5	-0.7	-0.8	-1.0
Focal spot size (nm)	66	78	89	82

Next, the geometry of MLFSL is discussed. In [17], Ramakrishna and Pendry have shown the principle of multilayer near field superlens. Thereby MLFSL model also obeys this principle. We shall denote  $N$  the number of slabs with negative dielectric constant in the alternating structure. Using (13), the transmittance with different thickness of slab, and  $N$  is calculated, as shown in Figure 3.

We obtain that the number of transmission resonances which depend on the number of surface states increases with increasing number of layers. With absorptive material, however, the transmission decays faster with  $k_x$  for larger  $k_x$  in the case of the thicker slabs (10 nm) than in the case of the thinner slabs (8 nm). This reconfirms the result [17] that the effects of absorption would be less deleterious for the image resolution in the case of thinner layers. And the distance between two arrays of multilayer thin flat silver slabs can be optimized by using rigorous coupled wave analysis (RCWA) [25–27]. So the

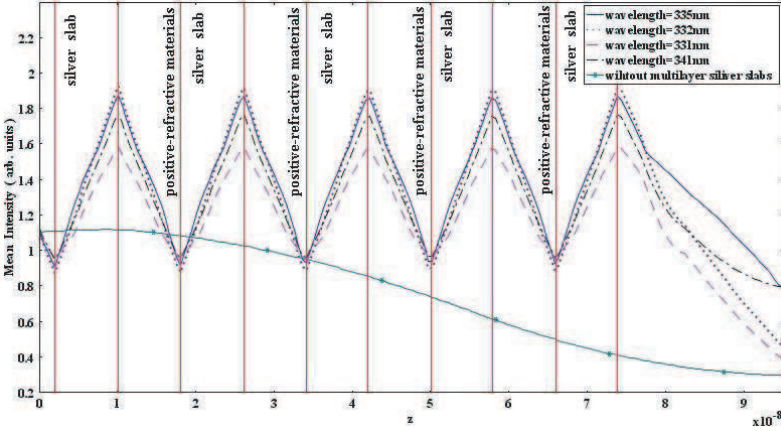
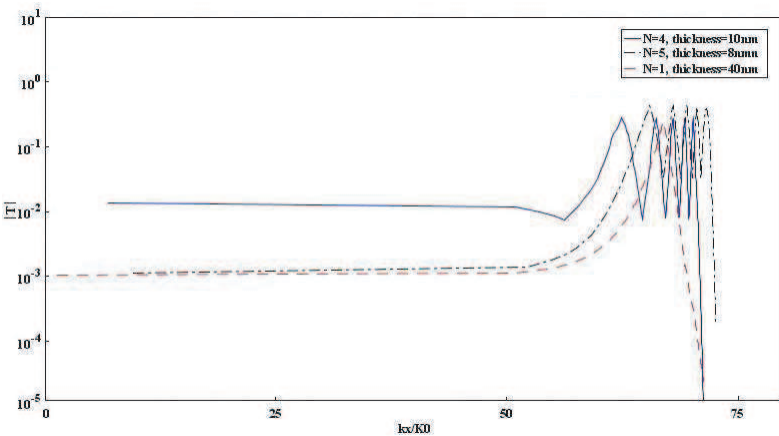


**Figure 2.** The integrated mean intensity of the multilayer Ag slabs superlens image.

computationally optimized geometry of the MLFSL is:  $a = b = 8 \text{ nm}$ ,  $c = 16 \text{ nm}$ ,  $d = 80 \text{ nm}$ ,  $e = f = 80 \text{ nm}$ ,  $g = 100 \text{ nm}$ , and the object is a double-slit structure, as shown in Figure 1.

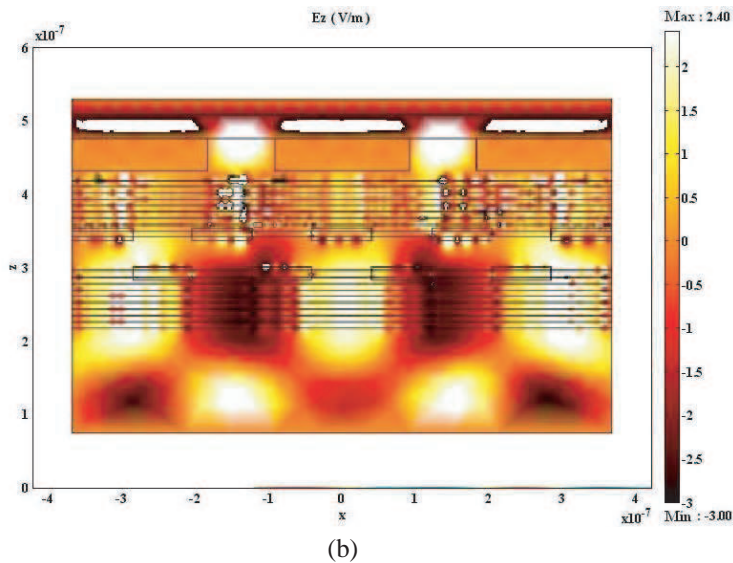
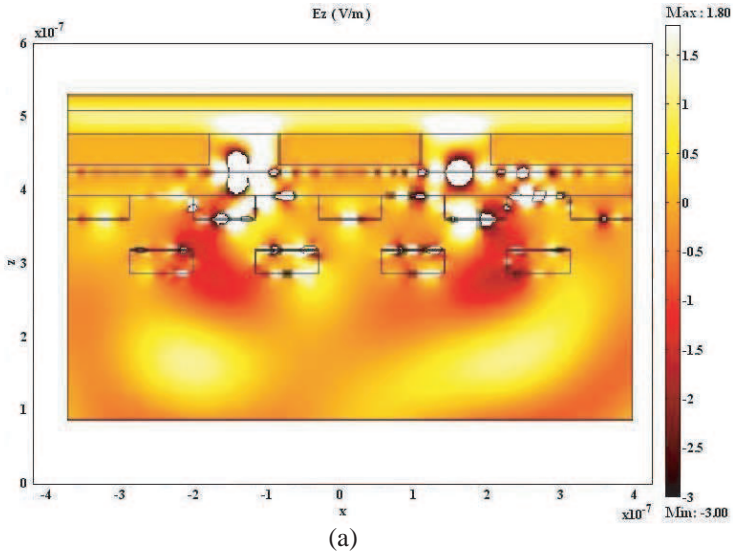
Figures 4(a) and (b) show the electric field intensity distribution of FSL and MLFSL, respectively. We can find that the field intensity of MLFSL is more concentrated than that of FSL. The generalized Optical Transfer Function (OTF) can be defined as

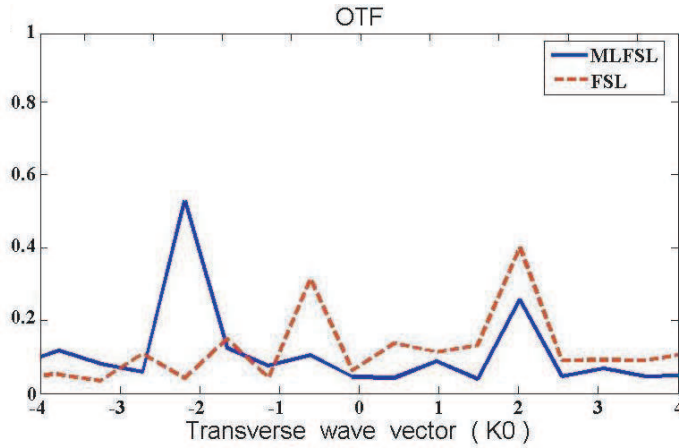
$$OTF = \frac{\tilde{H}_{img}}{\tilde{H}_{obj}} \tag{15}$$



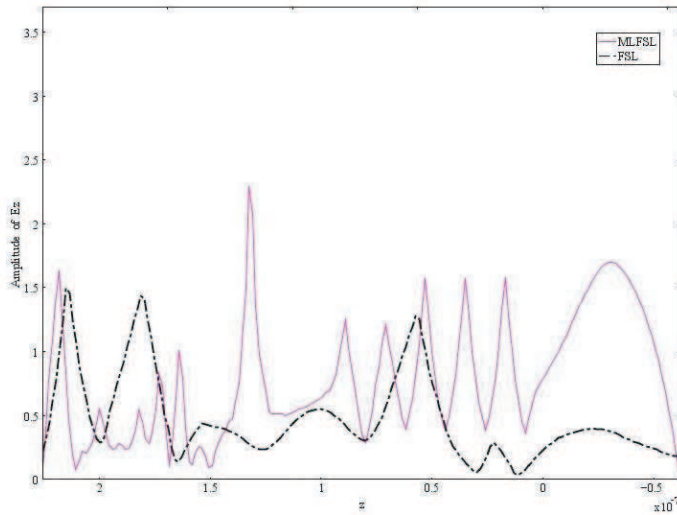
**Figure 3.** The transmittance of different slab thickness and  $N$ .

where  $\tilde{H}_{obj}$  is the Fourier transfer of source object and  $\tilde{H}_{img}$  Fourier transfer of (11). The COMSOL data are substituted back in (15), and then the OTF of MLFSL and FSL are obtained by using Matlab, as shown in Figure 4(c). In contrast, the evanescent waves from the object gain significant enhancement by the excitation of surface plasmon in the multilayer thin silver slabs and subsequently are converted into





(c)



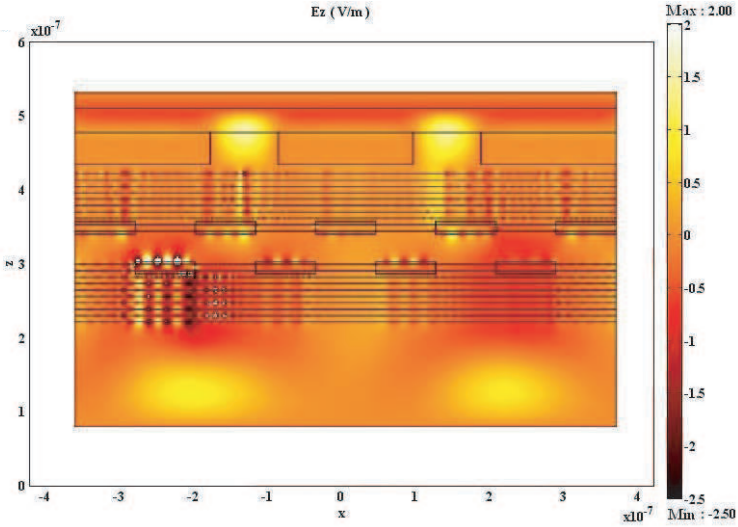
(d)

**Figure 4.** (a) The electric fields intensity distribution of FSL, (b) the electric fields intensity distribution of MLFSL, (c) OTF of MLFSL and FSL, and (d) the spatial distribution amplitude of  $E_z$ .

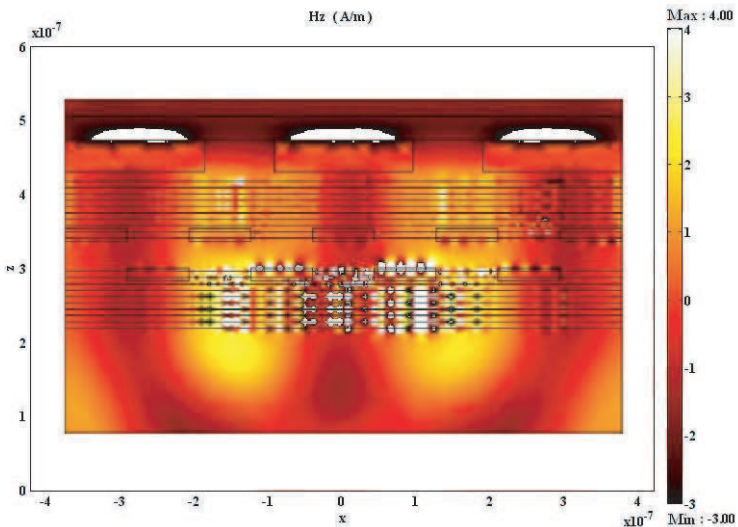
measurable propagating waves at the far field. Figure 4(d) shows the spatial distribution of the steady-state amplitude of  $E_z$  along the  $z$ -axis as a result of an evanescent wave interacting with silver slabs for MLFSL and FSL. The most important feature revealed by the figure is that the amplification of the evanescent wave of MLFSL is stronger

than that of FSL. The reason is that the effects of absorption will be less, and evanescent wave will be amplified by MLFSL model.

In order to study the influence of the incident angle on MLFSL, 1st-order electric and magnetic fields intensity with  $75^\circ$  incident angle are computed. The best oblique incident angle scope to OAI has been concerned in our previous work [19], as shown in Figures 5–6.



(a)



(b)

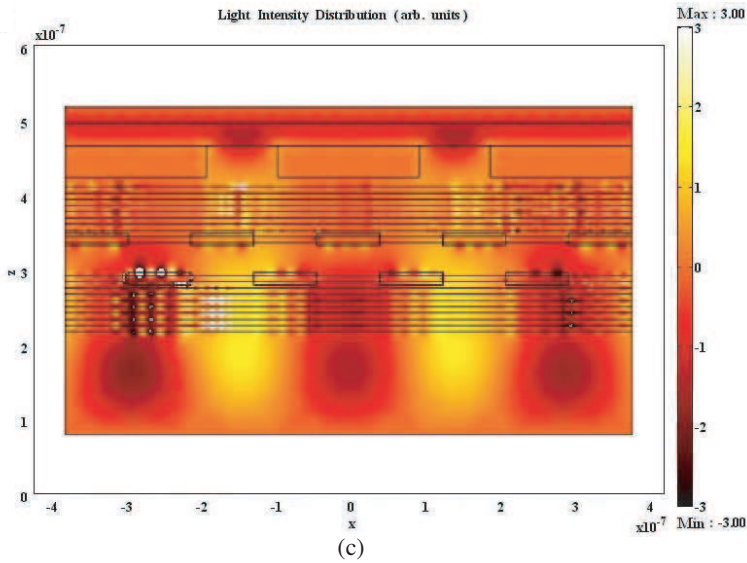


**Figure 5.** (a) The electric fields intensity distribution of MLFSL with  $75^\circ$  incident angle in TE-polarization, (b) magnetic fields intensity distribution of MLFSL with  $75^\circ$  incident angle in TM-polarization, (c) the intensity profile by combining (a) and (b).

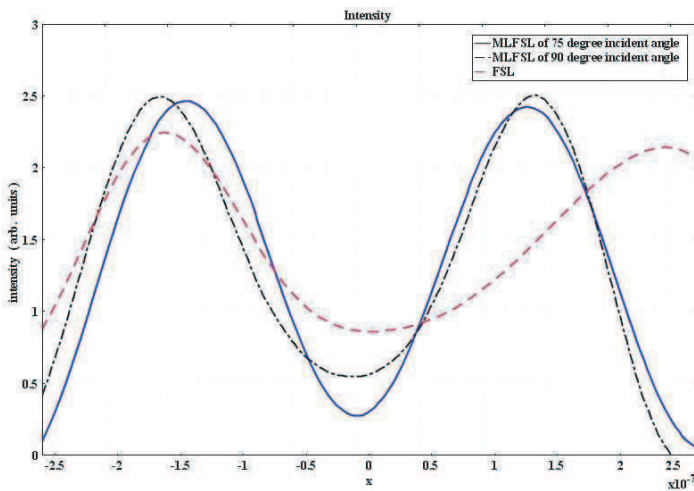


**Figure 6.** The light intensity distribution of MLFSL and FSL.

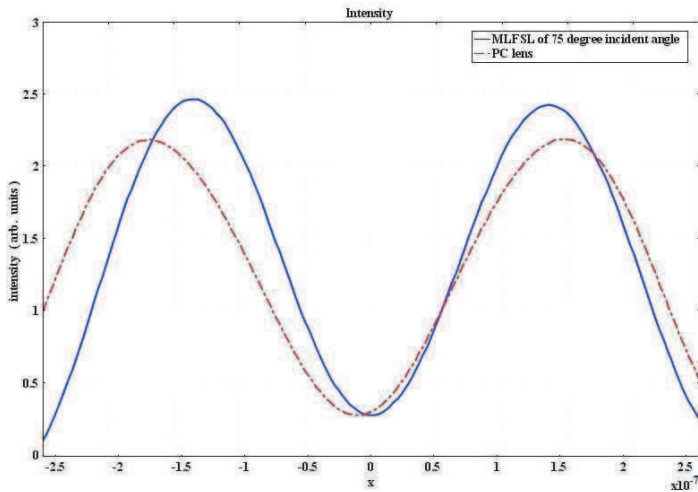


**Figure 7.** The light intensity distribution of MLFSL and PC.

Figures 5(a) and (b) show the electric and magnetic fields intensity distribution of MLFSL under  $75^\circ$  incident angle in TE- and TM-polarizations, respectively, and (c) shows the intensity profile by combining (a) and (b). Using the OAI, we have also successfully imaged the pattern of object. To quantify the effectiveness of the far-field imaging, the light intensity distributions located in image plane are compared as shown in Figure 6. The distance between the bottom of MLFSL and the imaging plane is the same as that of FSL which is defined as far-field region [15, 26]. Whether the double-slit can be distinguished in the image plane is dependent on the minimum value of intensity at the central location. So the the resolution enhancement of the MLFSL under oblique illumination is evident from the Figure 6. For strong polarization with OAI, the evanescent waves from the object gain significant enhancement by the excitation of surface plasmon in the MLFSL model. Combining both TE and TM polarizations under oblique illumination, MLFSL can capture simultaneously both propagation and evanescent bands in a single measurement with full bandwidth of  $2k_c$  and project a subdiffraction image that allows real-time imaging.

Finally, compared with a photonic crystal lens (PC) with a negative refractive index [28, 29], the intensity distributions are shown as Figure 7. The PC model is from [29]. The image contrast of these lenses is computed by the following formula:

$$C = \frac{I_{\max} - I_{\min}}{I_{\max} + I_{\min}} \tag{16}$$

The image contrast of MLFSL is about 0.79, and that of PC is about 0.75. So the imaging quality of MLFSL is much better.

#### 4. CONCLUSION

A new MLFSL is firstly proposed in this manuscript. It is made of the array structure of positive- and negative-refractive-index media and periodic corrugations. The MLFSL takes advantage of the multilayer stack to minimize the intrinsic absorption by surface plasmon resonances of multilayer slabs and can image effectively. The essential function of our model lies in its ability to excite of surface plasmon by multilayer thin silver slabs under oblique illumination, which can significantly enhance evanescent waves. The simulation results show that MLFSL under OAI is capable of far-field optical imaging beyond the diffraction limit. The multilayer far-field superlens optical imaging under OAI has great potential for many exciting applications in optical imaging, electronics manufacturing, and biomedical sensing.

#### REFERENCES

1. Veselago, V. G., "Properties of materials having simultaneously negative values of dielectric ( $\epsilon$ ) and magnetic ( $\mu$ ) susceptibilities," *Sov. Phys. Solid State*, Vol. 8, 2854–2856, 1967.
2. Pendry, J. B., "Negative refraction makes a perfect lens," *Phys. Rev. Lett.*, Vol. 85, 3966, 2000.
3. Zhang, Y., T. M. Grzegorzczuk, and J. A. Kong, "Propagation of electromagnetic waves in a slab with negative permittivity and negative permeability" *Progress In Electromagnetics Research*, PIER 35, 271–286, 2002.
4. Srivastava, R., S. Srivastava, and S. P. Ojha, "Negative refraction by photonic crystal," *Progress In Electromagnetics Research B*, Vol. 2, 15–26, 2008.
5. Mahmoud, S. F. and A. J. Viitanen, "Surface wave character on a slab of metamaterial with negative permittivity and permeability," *Progress In Electromagnetics Research*, PIER 51, 127–137, 2005.
6. Podolskiy, V. A., A. K. Sarychev, and V. M. Shalaev, "Resonant light interaction with plasmonic nanowire systems," *Opt. Express*, Vol. 11, 735, 2003.
7. Linden, S., C. Enkrich, M. Wegener, J. Zhou, T. Koschny, and C. M. Soukoulis, "Magnetic response of metamaterials at 100 Terahertz," *Science*, Vol. 306, 1351, 2004.

8. Zhang, S., W. Fan, B. K. Minhas, A. Frauenglass, K. J. Malloy, and S. R. J. Brueck, "Midinfrared resonant magnetic nanostructures exhibiting a negative permeability," *Phys. Rev. Lett.*, Vol. 94, No. 3, 2005.
9. Dolling, G., M. Wegener, C. M. Soukoulis, and S. Linden, "Negative-index metamaterial at 780 nm wavelength," *Opt. Lett.*, Vol. 32, 53–55, 2007.
10. Lezec, H. J., J. A. Dionne, and H. A. Atwater, "Negative refraction at visible frequencies," *Science*, Vol. 316, 430, 2007.
11. Shi, L., L. Gao, S. He, and B. Li, "Superlens from metal-dielectric composites of nonspherical particles," *Phys. Rev. B*, Vol. 76, No. 4, 045116, 2007.
12. Ambati, M., N. Fang, C. Sun, and X. Zhang, "Surface resonant states and superlensing in acoustic metamaterials," *Phys. Rev. B*, Vol. 75, 195447, 2007.
13. Cai, W., D. A. Genov, and V. M. Shalaev, "A superlens based on metal-dielectric composites," *Phys. Rev. B*, Vol. 72, 193101, 2005.
14. Rao, X. S. and C. K. Ong, "Subwavelength imaging by a left-handed material superlens," *Phys. Rev. E*, Vol. 68, 067601, 2003.
15. Liu, Z., S. Durant, H. Lee, Y. Pikus, N. Fang, Y. Xiong, C. Sun, and X. Zhang, "Far-field optical superlens," *Nano Letters*, Vol. 7, No. 2, 403–408, 2007.
16. Lee, H., Z. Liu, Y. Xiong, C. Sun, and X. Zhang, "Design, fabrication and characterization of a far-field superlens," *Solid State Communications*, Vol. 146, 202–207, 2008.
17. Ramakrishna, S. A. and J. B. Pendry, "Imaging the near field," *Journal of Modern Optics*, Vol. 50, No. 9, 1419–1430, 2003.
18. Inazuki, Y. C., "Analysis of diffraction orders including mask topography effects for OPC optimization," *Proc. of SPIE on Optical Microlithography XX*, Vol. 6520, 65204S, San Jose, CA, USA, 2007.
19. Cao, P., L. Cheng, and X. Zhang, "Vector hopkins model research based on off-axis illumination in nanoscale lithography," *Progress In Electromagnetics Research*, PIER 93, 291–306, 2009.
20. Born, M. and E. Wolf, *Principles of Optics*, Pergamon Press, 1980.
21. Lee, K., H. Park, J. Kim, G. Kang, and K. Kim, "Improved image quality of a Ag slab near-field superlens with intrinsic loss of absorption," *Optics Express*, Vol. 16, No. 3, 1711–1718, 2008.
22. Pendry, J. B., A. J. Holden, D. J. Robbins, and W. J. Stewart, "Magnetism from conductors and enhanced nonlinear phenomena," *IEEE Trans. Microw. Theory. Tech.*, Vol. 47, No. 11,

- 1084–2075, Nov. 1999.
23. Feng, L., X.-P. Liu, M.-H. Lu, and Y.-F. Chen, “Phase compensating effect in left-handed materials,” *Physics Letters A*, Vol. 332, 449–455, 2004.
  24. Pokrovsky, A. L. and A. L. Efros, “Lens based on the use of left-handed materials,” *Appl. Opt.*, Vol. 42, 5701–5705, 2003.
  25. Xiong, Y., Z. Liu, and X. Zhang, “Far-field superlens imaging at visible wavelengths,” *SPIE Newsroom*, 2008.
  26. Durant, S., Z. Liu, J. M. Steele, and X. Zhang, “Theory of the transmission properties of an optical far-field superlens for imaging beyond the diffraction limit,” *J. Opt. Soc. Am. B*, Vol. 23, No. 11, 2383–2392, 2006.
  27. Moharam, M. G., E. B. Grann, D. A. Pommet, and T. K. Gaylord, “Formulation for stable and efficient implementation of the rigorous coupled-wave analysis of binary gratings,” *J. Opt. Soc. Am. A*, Vol. 12, 1068–1076, 1995.
  28. Pandey, G. N., K. B. Thapa, S. K. Srivastava, and S. P. Ojha, “Band structures and abnormal behavior of one dimensional photonic crystal containing negative index materials,” *Progress In Electromagnetics Research M*, Vol. 2, 15–36, 2008.
  29. Moussa, R., S. Foteinopoulou, L. Zhang, G. Tuttle, K. Guven, E. Ozbay, and C. M. Soukoulis, “Negative refraction and superlens behavior in a two-dimensional photonic crystal,” *Physical Review B*, Vol. 71, 085106, 2005.